Arch. Metall. Mater. **71** (2026), 3, 787-792

DOI: https://doi.org/10.24425/amm.2026.1968

JAN KUSIŃSKI[1*], ŁUKASZ CIENIEK[1]

CALCIUM DOPING IN RROCK-SALT TRANSITION METAL OXIDES: DEFECT STRUCTURE, MICROSTRUCTURAL EVOLUTION, AND TRANSPORT PROPERTIES IN FeO, CoO, AND NiO

This review presents the results of experimental study conducted over three decades on calcium doping in three isostructural iron-group rock-salt oxides: wüstite (Fe_{1}–δO), cobalt (CoO), and nickel (NiO) monoxides. In the case of calcio-wüstite, the large Ca^{2+}/Fe^{2+} ionic radius mismatch (1.00 vs 0.77 Å) lowers the stacking fault energy, generating ordered stacking faults that transform into $CaFe_5O_7$ ferrite precipitates during reduction in CO atmosphere. In Ca-doped cobalt oxide single crystals, oxygen activity controls extensive precipitation of Ca-free Co_3O_4 spinel which electron energy-loss spectroscopy links to changes in the Co^{3+}/Co^{2+} ratio and to the abrupt conductivity decrease for the partial pressure of oxygen near $p \approx 10^{-3}$-10^{-4} atm. In Ca-doped nickel oxide, CaO-rich eutectic-like zones form near subgrain boundaries without precipitation of spinels The chemical diffusion and electrical field kinetic demixing experiments have been combined to prove that the presence of Ca leads to an increase of the chemical diffusion coefficient of NiO. This unexpected result ($D(Ca^{2+}) > D(Ni^{2+})$), confirmed during electrical conductivity experiment, indicates that correlation effects between Ni and Ca cations play a decisive role in diffusion processes in (Ni,Ca)O.

The study were conducted using TEM, SEM, ELELS, TML and EDS techniques, as well electrical conductivity measurements.

Keywords: Ca-doped FeO, CoO and NiO; microstructure; spinel precipitation; transport properties; electrical conductivity

1. Introduction

Wüstite (Fe_{1}–δO), CoO, and NiO share the rock-salt structure and p-type semiconducting behaviour based on hole hopping [1-3] but their defect landscapes differ significantly: wüstite sustains large non-stoichiometries ($\delta \leq 0.15$) with complex vacancy clusters [3], CoO has 4:1 clusters that nucleate spinel whereas: NiO is dominated by isolated cation vacancies with no clustering tendency [2]. Ca^{2+} doping provides a controlled probe because Ca^{2+} is isovalent yet substantially larger than all three host cations ($r \approx 1.00$ Å compared to 0.77, 0.745, and 0.69 Å for Fe^{2+}, Co^{2+}, and Ni^{2+}, respectively), so its elastic size mismatch interacts with each host's defect structure in a characteristically different manner [1-3]. This review synthesizes five investigations conducted in the AGH University of Krakow, CNRS Bellevue Meudon and École Centrale Paris, covering partial reduction of Ca-doped wüstites [5-7], crystal growth and spinel-formation in (Co,Ca)O [8-9], a comprehensive parametric study of (Co,Ca) O microstructural evolution [8-10], as well microstructure and transport coupling in Ca-doped NiO [11].

2. Experimental

CaO-doped monocrystalline CoO (1, 1.7, 5, and 10 mol.% CaO) and NiO (2 and 2.65 mol.% CaO) samples were grown by the crucible-free floating-zone technique (CYBERSTAR apparatus) using high purity CoO, NiO and CaO-bearing oxide rods pressed at 400 MPa [4]. Growth was seeded on pre-oriented [001] crystals: all single crystals were homogenized at 1200°C/100 h after growth, (Figs. 1 and 2). Wüstite samples were prepared by oxidation of high-purity polycrystalline Armco iron plates at 1150, 1200, and 1260°C for eight days, yielding wüstite scales of controlled stoichiometry. Then, wüstite crystals were milled to get fine powder and formed by pressing to the form of rods (ϕ = 6 mm, l = 50 mm). Monocrystalline samples of pure wüstite were grown by the crucible-free floating-zone technique described above. Calcio-wüstite were received by thermochemical calcium doping that was achieved by annealing the wüstite in contact with pure CaO powder at 900°C for four hours in a 50 vol.% CO / 50 vol.% CO_2 atmosphere, yielding homogenous samples with Ca concentrations of 0.82-0.85 wt.%, as confirmed by Camebax electron probe microanalysis. Fol-

[1] AGH UNIVERSITY OF KRAKOW, FACULTY OF METALS ENGINEERING AND INDUSTRIAL COMPUTER SCIENCE, AL. A. MICKIEWICZA 30, 30-059 KRAKOW, POLAND

* Corresponding author: kusinski@agh.edu.pl

lowing doping, samples were homogenised at 900°C for four days. Reduction was conducted at 900°C and 1000°C in pure CO atmosphere for durations ranging from 30 s to two hours, followed by rapid quenching.

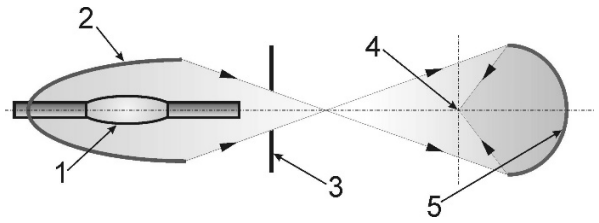

Fig. 1. Schematic diagram of single crystal preparation device (CYBERSTAR); 1 – high intensity xenon lamp, 2 – elliptic mirror, 3 – movable diaphragm, 4 – the focal point of reflected beam (point where in melting chamber the nucleus and the sample are placed), 5 – parabolic mirror [4]

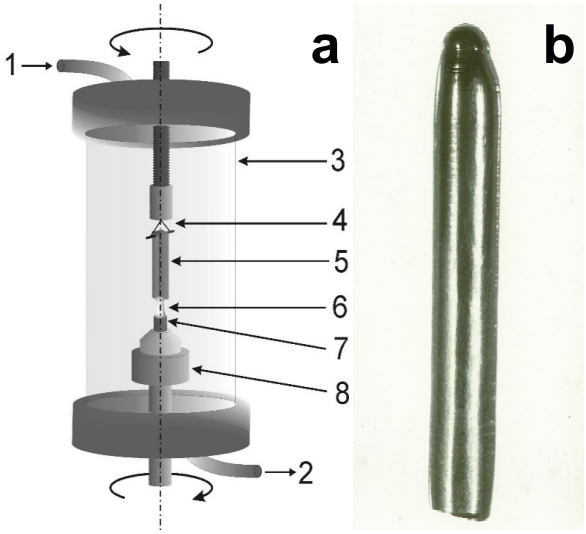

Fig. 2. Schematic diagram of melting chamber – a (1, 2 – the system of protective gas inlet and outlet, (the air pumping in case of running with vacuum), 3 – the glass tube, 4 – the system of fixing (hanging) and turning of the sample, 5 – sample, 6 – melted zone, 7 – nucleus, 8 – the system of fixing and turning of nucleus and) and (Co,Ca)O monocrystal – b [4]

Optical transmission light microscopy (TLM) provided mesoscale survey information. SEM with energy-dispersive X-ray spectroscopy (EDS) was used for surface morphology and composition mapping. TEM was performed using JEOL 200CX and Philips CM20-UltraTwin (120 kV) instruments; the latter was also used for EELS. Thin foils for TEM examinations were prepared from slices of the massive reduced and non-reduced samples cut with a Struers diamond saw perpendicularly to their surface. 3 mm discs were cut from the slices, thinned by mechanical polishing and dimpling to a thickness of 30-60 mm, chemically polished in hot orthophosphoric acid and finally ion-milled. Monitoring of the CoO ⇔ Co_3O_4 phase boundary and lattice parameter evolution was performed in air using high-temperature X-ray. Seebeck coefficient and electrical conductivity were measured simultaneously as functions of temperature (1000-1200°C) and p_{O_2}

3. Results and discussion

3.1. Ca-doped wüstite: stacking faults and reduction behaviour

The microstructure of undoped wüstite is well established: TEM reveals only a few dislocations in the matrix, and the [100] electron diffraction pattern shows superstructure spots characteristic of the ordered vacancy-cluster arrangement, but no planar defects [5,6]. Calcium doping leads to a qualitatively different microstructure due to the significantly larger ionic size of calcium compared to iron ($r(Ca^{2+}) \approx 1.00$ Å, $r(= Fe^{2+}) = 0.77$ Å) which consequently introduces elastic strain that lowers the stacking fault energy of $Fe_{1-\delta}O$. A high density of extrinsic stacking faults accordingly appears in the matrix, arranged in an ordered, cross-hatched pattern on {001} planes (Fig. 4) [5-7]. Dark-field imaging (Fig. 4b) with $g = 020$ confirms the extrinsic character of the faults in accordance with Gevers' criterion [12]. The physical origin of the stacking fault proliferation is the Suzuki mechanism [13] according to which, solute atoms whose size is incompatible with the host atoms preferentially segregate to stacking fault planes. Due to this, local lattice relaxation at this location reduces the elastic misfit energy of the oversized solute, thereby lowering the fault energy and stabilising the planar defect. Atoms of Ca^{2+}, with its 0.23 Å mismatch relative to Fe^{2+}, largely satisfies this condition. X-ray microanalysis (Ca-K area scan) of calcio-wüstite

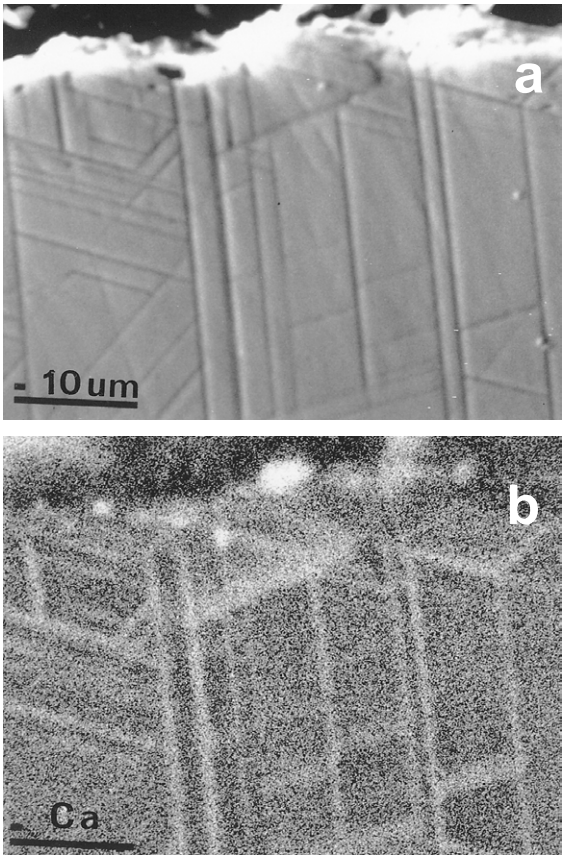

Fig. 3. SEM image of stacking faults at the surface of layer of wüstite after thermochemical treatment in Ca powder at 900°C for 1 h and corresponding Ca elemental map [7]

after thermochemical treatment in CaO powder at 900°C for one hour shows a pronounced Ca enrichment at the wüstite surface (Fig. 3), confirming the strong kinetic tendency of Ca^{2+} towards interfacial accumulation. During reduction in CO at 900-1000°C, iron is selectively removed because the formation enthalpy of FeO is much lower than that of CaO, which therefore remains in the wüstite lattice. The low solubility of Ca in metallic iron (approximately 0.05 wt.%) causes Ca^{2+} cations to accumulate ahead of the advancing reduction front rather than partition into the growing iron layer. Quantitative microprobe Ca concentration profiles measured after reduction at 900°C for 15, 30, and 60 min [5-7] reveal a dynamic, time-evolving Ca enrichment extending up to 100 μm ahead of the iron/wüstite interface and growing progressively with reduction time. This dynamic segregation arises from the coupling of four simultaneous fluxes within the wüstite: electron holes ($h^{\cdot}$) migrating away from the reduction front; cation vacancies (V''_{Fe}) flowing towards it; Fe^{2+} cations moving to be consumed; and Ca^{2+} cations redistributed through the cation vacancy sublattice [5-7]. The mechanism is formally equivalent to kinetic demixing. Concurrently, the characteristic stacking-fault fringe contrast visible in Fig. 4 progressively weakens and disappears in TEM images taken closer to the reduction front (Fig. 5a): once incoherent ferrite nucleates on the fault plane, the crystallographic periodicity responsible for the fringe image is disrupted and the contrast disappears. As Ca^{2+} concentration at the stacking faults ahead of the reduction front exceeds approximately 1.5 wt.%, the faults become so enriched that thin, plate-like $CaFe_5O_7$ calcium ferrite precipitates nucleate directly on the fault planes (Fig. 5b and 6b). Their crystal

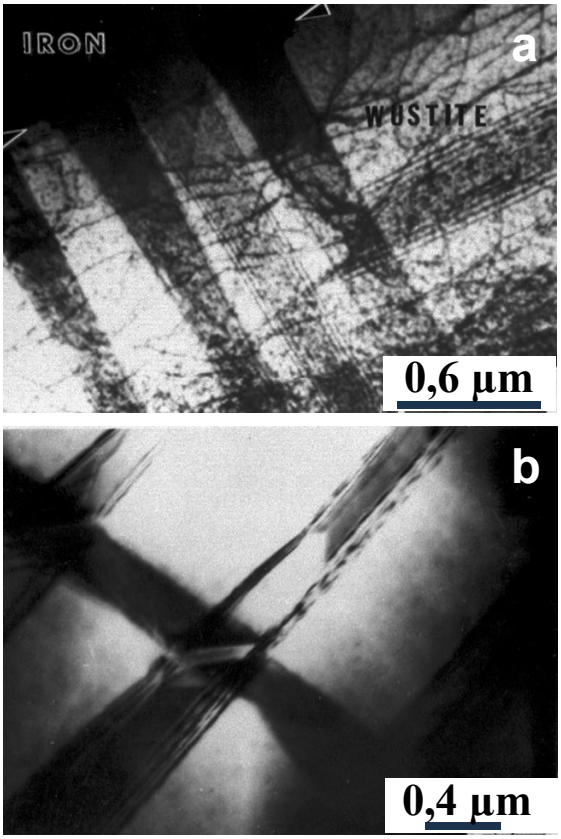

Fig. 5. TEM images showing changes of the stacking faults microstructure at the front of reduction. Highdislocation density (a), and plate-like precipitates formed at the stacking faults due to the Ca segregation (b) were observed [7]

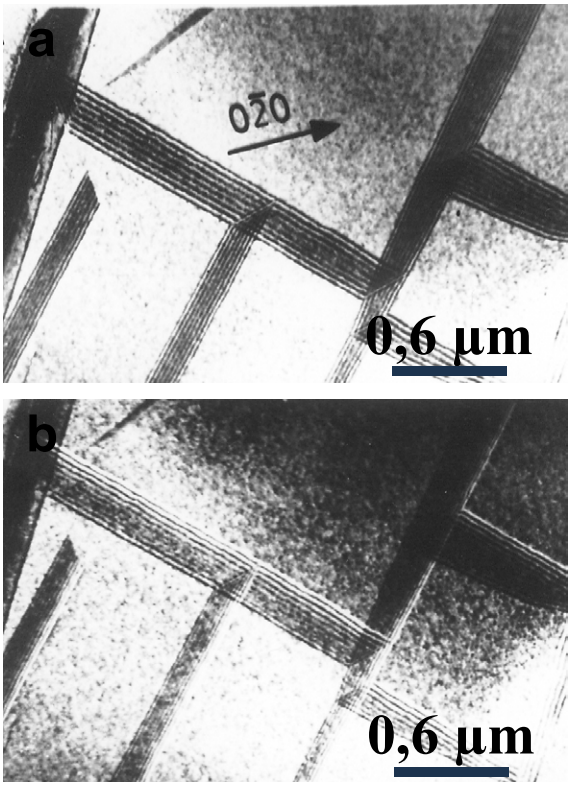

Fig. 4. TEM images of (bright – a and dark – b field imaging of 002 reflection) of stacking faults observed in calcio-wüstite [5]

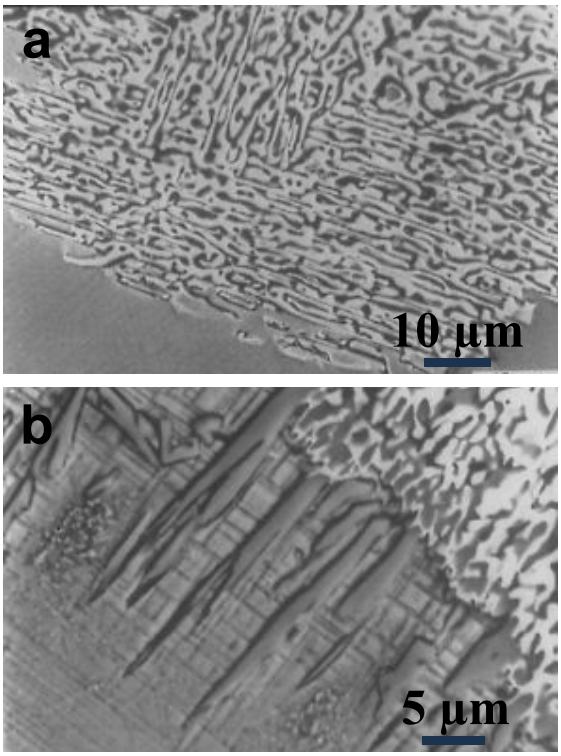

Fig. 6. SEM images of the reduced iron/calcio- wüstite interface after reduction at 1000°C for 2 h. Reduced area of the sample (a) and calcio-ferrite precipitates at the stacking faults due to Ca segregation at the reduction front (b), [7]

structure was confirmed by electron diffraction, and their mutual orientation – parallel to the parent stacking fault planes – confirms a topotactic relationship between fault and precipitate.

3.2. Ca-doped CoO: Co_3O4 spinel precipitation and conductivity

Argon-annealed samples ($pO_2 \approx 10^{-6}$ atm) are essentially precipitate-free (Fig. 7a) [8-11], apart from very fine (square-like) precipitates, decorating the subgrain boundaries, and the areas of a high density of dislocations (Fig. 7a). Air annealing drives prolific Co_3O_4 precipitation amplified by Ca content (Figs. 7b and 8) [8]. These precipitates are regular squares or rectangles surrounded by dislocations of high density. The dark-field image (Fig. 8b) shows intensive precipitation of ultrafine particles in the matrix, around large plate-like precipitates. The EELS and EDS confirm the precipitates are Ca-free due to the diffusion of Ca^{2+} cations into the surrounding matrix during nucleation [8-11]. At 1-1.7 mol.% CaO, precipitates are compact polycrystalline squares or rectangles on {001} planes (Figs. 7b and 8), with Moiré fringes confirming early coherency. The precipitation morphology is very sensitive to the concentration of Ca atoms and to the partial pressure of oxygen. At 5-10 mol.% CaO they elongate into plate-like morphologies [9,10]. EELS confirms atmosphere-driven cobalt valence changes, as indicated by the following experimental results: the Co L_3/L_2 ratio is higher in argon-annealed matrix ($R_g \approx 2.39$) than in air ($R_g \approx 2.32$); the Co L_3/L_2 spin-orbit splitting increases from 19.4 eV to 23.4 eV; and O K and Co L_{23} edges shift to higher energy losses under oxidizing conditions [9]. High-temperature X-ray diffractometry on CoO + 5 mol.% CaO in air shows Co_3O_4 persisting to at least 1370 K, beyond the accepted CoO–CaO boundary [10]. Conductivity of (Co,Ca)O decreases abruptly near $pO_2 \approx 10^{-3}$-10^{-4} atm [9,10], linked to Co_3O_4 dissolution and collapse of the Co^{3+}/Co^{2+} ratio; below this range, sub-Co^{2+} species are proposed to predominate, further reducing hole concentration, absent in pure CoO, confirming the essential role of Ca^{2+}.

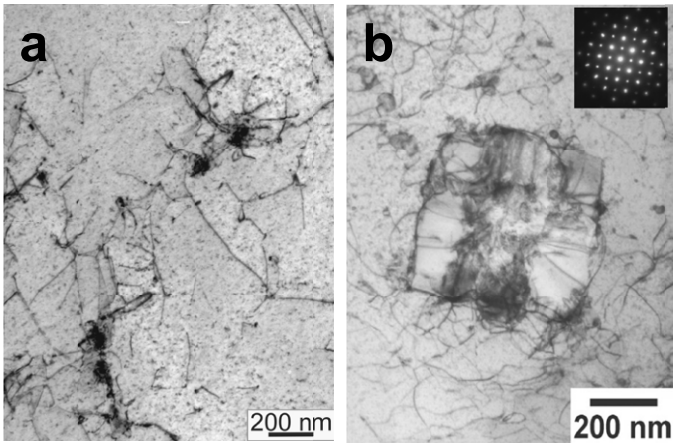

Fig. 7. Microstructure of the (Ca,Co)O; 1.7 mol.% CaO; a – sample annealed at 1100°C for 2 h in air, b – sample annealed at 1100°C for 2 h in argon [10]

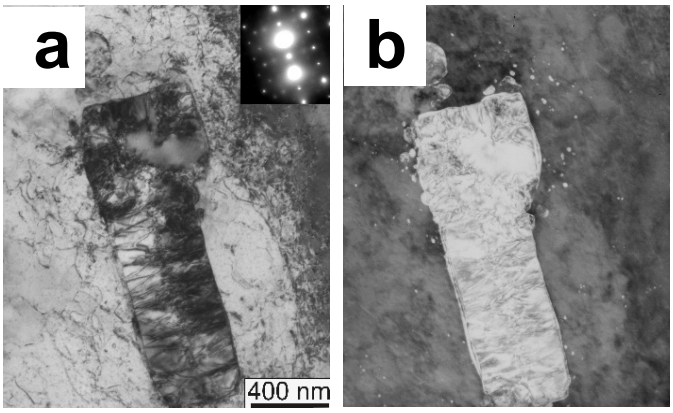

Fig. 8. Microstructure of the (Ca,Co)O sample annealed at 1100°C for 2 h in air: (a) bright-field image; (b) dark-field image; 1.7 mol.% CaO [10]

3.3. Ca-doped NiO: CaO precipitation and anomalous Ca^{2+} diffusivity

TEM and EDS of (Ni,Ca)O reveal exclusively CaO precipitates near subgrain boundaries across the entire p_{O_2} range (air to 10^{-10} atm); no spinel is detected. The fibrous eutectic-like morphology at high oxygen activities (Fig. 9) – predicted by the NiO–CaO diagram only near 42 mol.% CaO at ≈1700°C [11] – confirms metastable formation by rapid quenching. Ca doping monotonically enhances NiO conductivity through hole augmentation by increasing the number of holes. Seebeck measurements confirm p-type behavior at 1000-1200°C. Under 0.5 V/mm at 1292°C for 60 days, EDS mapping reveals Ca enrichment at the cathode and porosity at the anode (Fig. 10), establishing $D(Ca^{2+}) > D(Ni^{2+})$. This anomalous mobility is due to the elastic Ca^{2+}–vacancy coupling, which raises effective vacancy-exchange rate Ca^{2+} cations above that of Ni^{2+} despite its larger radius.

4. Conclusions

In calcio-wüstite, Ca^{2+} lowers the stacking fault energy via the Suzuki mechanism, generating ordered stacking faults that transform into $CaFe_5O_7$ ferrite platelets above ≈1.5 wt.% Ca during CO reduction. Dynamic Ca^{2+}–vacancy flux coupling accumulates Ca^{2+} ahead of the reduction front, producing a porous iron morphology that accelerates reduction kinetics.

In Ca-doped CoO, p_{O_2} and Ca content jointly control abundance and morphology of Ca-free Co_3O_4 spinel. Spinel formation raises the Co^{3+}/Co^{2+} ratio and enhances hole-mediated conductivity; its dissolution at low pO_2 drives an abrupt conductivity decrease. Co_3O_4 persists at least to a temperature 1370 K, which is beyond the accepted CoO–CaO phase diagram boundary.

In Ca-doped NiO, no spinel forms across the entire pO_2 range range investigated. CaO eutectic-like zones appear near subgrain boundaries under all atmospheres used. Ca doping monotonically enhances conductivity.

The type of second-phase microstructure, stacking faults in FeO, spinel in CoO, CaO eutectic zones in NiO, dependence on

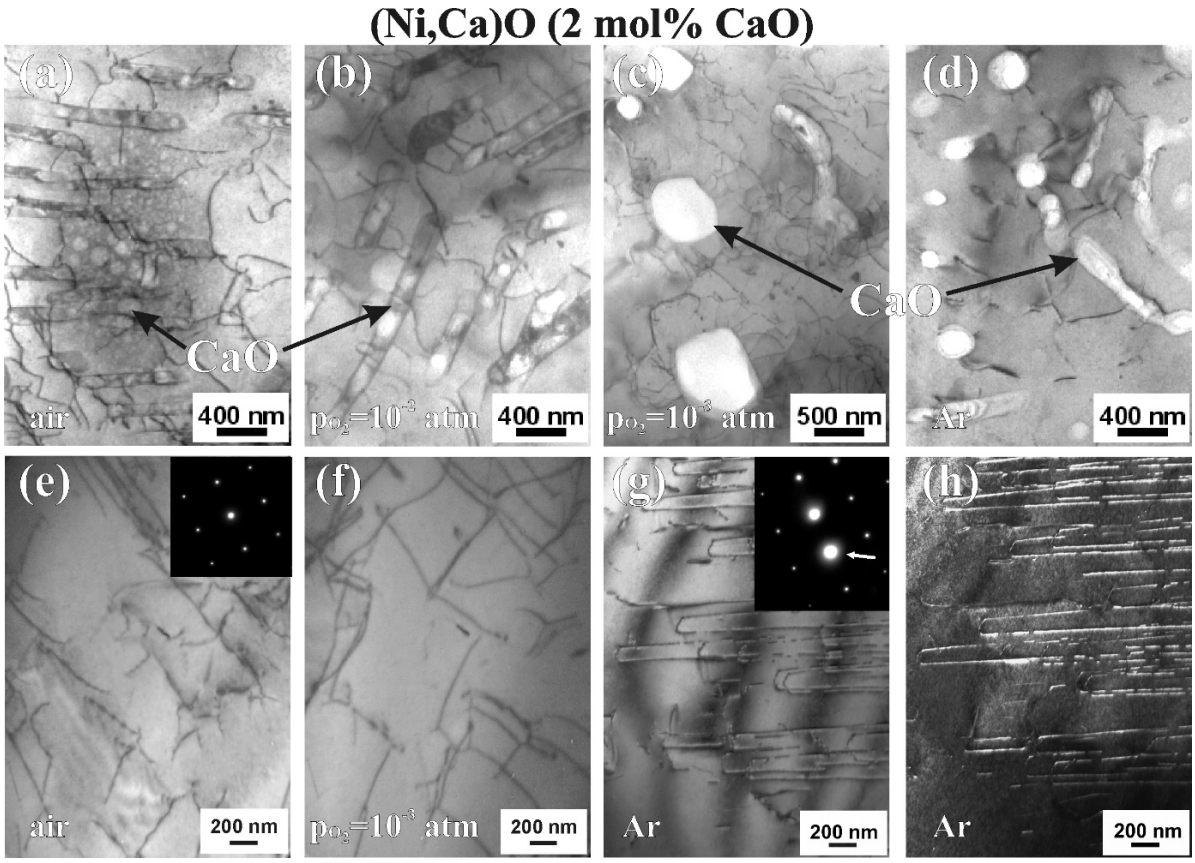

Fig. 9. Transmission electron microscopy images showing the microstructure of Ca-doped NiO (2 mol.% CaO) samples annealed at 1100°C for 2 h under different air pressure and rapidly quenched. Images (a)-(d) represent the region of eutectic-like precipitates observed near subgrain boundaries by TLM, and images (e)-(h) show the area between precipitates (free of particles). Images (g) and (h) are adequately bright-field and dark-field images of the same structure [11]

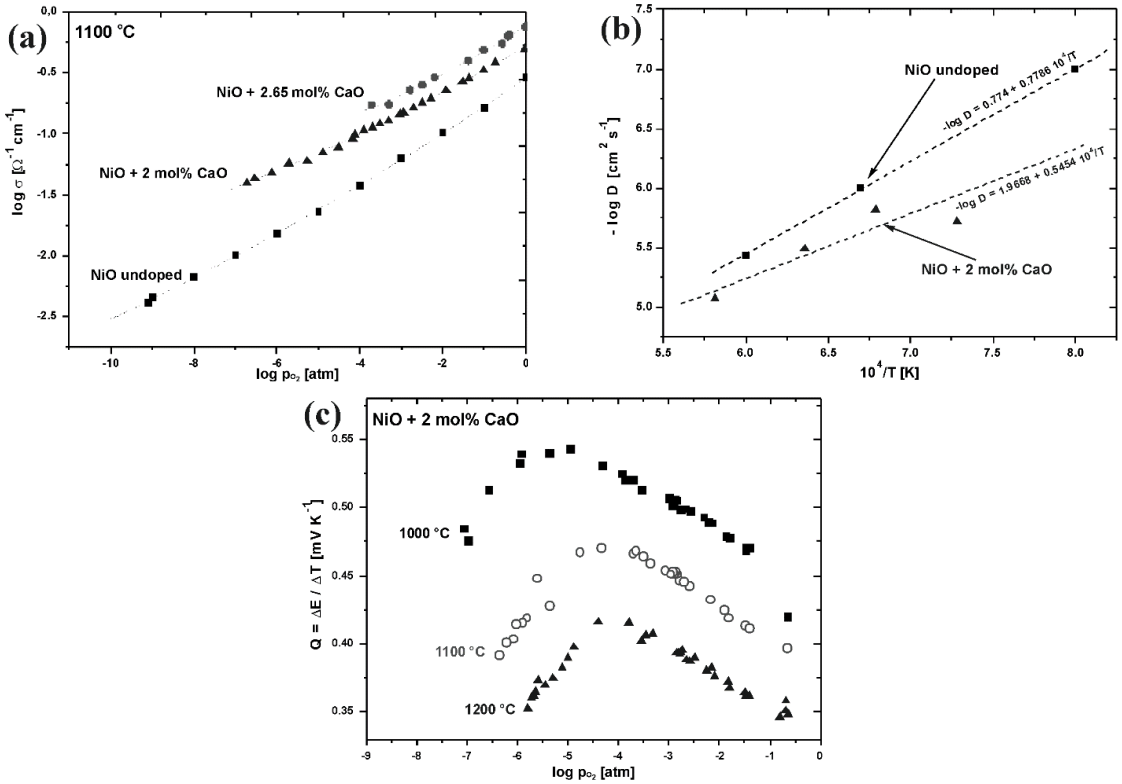

Fig. 10. Results of transport properties experiments showing that the increase of Ca content leads to increase of the electrical conductivity of (Ni,Ca)O with decrease of NiO stability range (a), and leads to an increase of chemical diffusion coefficient (b). Seebeck's effect measurements for (Ni,Ca)O (c) showing high temperature transport properties as an p-type semiconductor in wide range of oxygen partial pressure (Q > 0) [11]

the internal geometry of the host cation's-cluster, and not solely on the chemical properties of the dopant. Ca^{2+} cations generally segregates to high-energy microstructural features as a results of anomalous mobility of Ca^{2+} cations-vacancy pairs.

Acknowledgements

The experimental work reported here was carried out in collaboration with S. Jasienska†, C. Monty†, G. Petot-Ervas, C. Petot, and G. Baldinozzi. Financial support was provided by AGH University of Science and Technology, Kraków, Poland, CNRS Bellevue-Meudon, and École Centrale Paris, Châtenay-Malabry, France.

REFERENCES

[1] P.A. Cox, Transition metal oxide – an introduction to their electronic structure and properties, International Series of Monographs on Chemistry, Claredon Press, Oxford, 27, 1995.

[2] O.T. Soerensen, Nonstoichiometric Oxides, Academic Press, 2012, ISBN: 9780323149808

[3] J.R. Gavarri, C. Carel, Nucleation and solubility of defect clusters in substituted wüstites. Phase Transit. B**14B**, 103-109 (1989). DOI: https://doi.org/10.1080/01411598908206877

[4] L. Cieniek, T. Didenko, J. Kusinski, Numerical modelling of CoO single crystals preparation process using floating-zone technique, Inzynieria Materiałowa **6**, 777-783 (2005).

[5] J. Kusinski, TEM analysis of the nature of stacking faults in calcio- wüstite. Journal of Trace and Microprobe Techniques **15** (4), 509-513 (1997).

[6] J. Kusinski, S. Jasienska, C. Monty, T. Orewczyk, Study of phase transformations in doped wüstite by electron microscopy. Metallurgy and Foundry **20**, 2 (1994), UDC.546. 723-31.001.5.669.1.017/.018

[7] J. Kusinski, S. Jasienska, C. Monty, Microstructural and microanalytical examinations of partially reduced doped wüstites. Solid State Ionics B6D8, 185-192 (1994). DOI: https://doi.org/10.1016/0167-2738(94)00039-u

[8] J. Kusinski, L. Cieniek, Influence of calcium doping on the structure and electrical properties of cobalt oxide. Hutland B70B 182-189 (2003).

[9] J. Kusinski, G. Petot-Ervas, C. Petot, B. Jouffrey, P. Schattschneider, Microstructure and nanochemistry of Ca-doped cobalt oxide single crystals. Mater. Chem. Phys. B81B 308-311 (2003). DOI: https://doi.org/10.1016/S0254-0584(02)00589-8

[10] J. Kusinski, L. Cieniek, G. Petot-Ervas, C. Petot, G. Baldinozzi, Influence of Ca content and oxygen partial pressure on microstructural evolution of (Co,Ca)O at elevated temperatures. J. Microscopy B224B (1), 30-33 (2006). DOI: https://doi.org/10.1111/j.1365-2818.2006.01650.x

[11] L. Cieniek, J. Kusinski, G. Petot-Ervas, C. Petot, Microstructure and high temperature transport properties of Ca-doped nickel oxide. J. Microscopy B237B (3), 329-332 (2010). DOI: https://doi.org/10.1111/j.1365-2818.2009.03253.x

[12] R. Gevers, A. Art, S. Amelinckx, Electron microscopic images of single and intersecting stacking faults in thick foils. Phys. Status Solidi B3B, 1563-1593 (1963). DOI: https://doi.org/10.1002/pssb.19630030606

[13] H. Suzuki, Chemical interaction of solute atoms with dislocations. Sci. Rep. Res. Inst. Tohoku Univ. BA4B, 455-463 (1952).